Differentiation of Crystals Associated With Arthropathies by Spectral Photon-Counting Radiography

A Proof-of-Concept Study

Florian Alexander Huber, MD, Fabio Becce, MD,† Spyridon Gkoumas, PhD,‡ Thomas Thüring, PhD,‡ Sylvain Steinmetz, MD,§ Igor Letovanec, MD,|| and Roman Guggenberger, MD**

Objectives: The aims of this study were to test whether spectral photon-counting radiography (SPCR) is able to identify and distinguish different crystals associated with arthropathies in vitro and to validate findings in a gouty human third toe ex vivo.

Materials and Methods: Industry-standard calibration rods of calcium pyrophosphate, calcium hydroxyapatite (HA), and monosodium urate (MSU) were scanned with SPCR in an experimental setup. Each material was available at 3 different concentrations, and a dedicated photon-counting detector was used for SPCR, whereas validation scans were obtained on a clinical dual-energy computed tomography (DECT) scanner. Regions of interest were placed on SPCR images and consecutive DECT images to measure x-ray attenuation characteristics, including effective atomic numbers (Z_{eff}). Statistical tests were performed for differentiation of Z_{eff} between concentrations, materials, and imaging modalities. In addition, a third toe from a patient with chronic gouty arthritis was scanned with SPCR and DECT for differentiation of MSU from HA.

Results: In both SPCR and DECT, significant differences in attenuation and Z_{eff} values were found for different concentrations among ($P < 0.001$) and between different materials ($P < 0.001$). Overall, quantitative measurements of Z_{eff} did not differ significantly between SPCR- and DECT-derived measurements ($P = 0.054$–0.412). In the human cadaver toe, gouty bone erosions were visible on standard grayscale radiographic images; however, spectral image decomposition revealed the nature and extent of MSU deposits and was able to separate it from bone HA by Z_{eff}.

Conclusions: Identification and differentiation of different crystals related to arthropathies are possible with SPCR at comparable diagnostic accuracy to DECT. Further research is needed to assess diagnostic accuracy and clinical usability in vivo.

Key Words: crystal arthropathies, gout, monosodium urate, radiography, spectral photon-counting radiography

(*Invest Radiol* 2020;00: 00–00)

Identification of chemical compounds among the broad spectrum of crystal-associated arthropathies is known to be crucial for successful long-term therapy.[1–3] Gout, as the most frequent crystal-associated disease with typical subcutaneous and juxta-articular tophi, is primarily diagnosed by polarized light microscopy where monosodium urate (MSU) crystals in aspirated synovial fluid or biopsied tissue[4,5] can be identified with high specificity. However, in cases with negative microscopy results but high clinical suspicion, further investigation by ultrasound imaging and in particular dual-energy computed tomography (DECT) is now recommended by the European League Against Rheumatism.[4]

Provided with a certain density threshold, DECT is known to reliably discriminate MSU-containing tophi from calcium-containing crystals such as calcium pyrophosphate (CPP) or calcium hydroxyapatite (HA).[4,6–10] Furthermore, utilization of spectral photon-counting (PC) detectors in CT has recently been proven to enable discrimination between different crystal suspensions even more accurately.[11,12] The basic principle behind PC techniques is the use of novel detectors that are capable of discriminating different x-ray photon energies. As materials interact differently with x-ray radiation, the energy levels of resulting photons vary depending on the atomic structure of the scanned object. Therefore, this principle has intensely been investigated over the past decades in material science.[13,14] However, CT-based examinations are associated with substantial radiation burden, which hampers suitability of CT for opportunistic screening or disease monitoring in vivo.[15] To improve this limitation in applicability, a variety of strategies are currently being discussed, most importantly the utilization of PC and machine learning in image reconstruction, which have already shown promising results regarding the reduction of dose without compromise on image quality.[16–18]

Plain radiography on the other hand is a comparably cheap modality with broad access and uses markedly less ionizing radiation compared with CT for both the body trunk as well as for the appendicular skeleton.[19,20] However, compared with DECT, it has a much lower diagnostic performance in detection of gouty tophi because of in-plane superposition of tissues and without the possibility of material decomposition based on attenuation at different energy levels.[4,21] This has gradually led to a decline of conventional radiography in the diagnosis of gout[4] and a controversially discussed role in CPP deposition disease.[22]

Nonetheless, after decades of constantly increasing the use of cross-sectional imaging, recent technologic innovations have sparked new interest in conventional radiography. Exemplarily, De Silvestro et al[23] have shown an added value of tomosynthesis in the field of musculoskeletal radiology, proving significantly better assessment of fracture healing in the hand and wrist, when compared with standard digital x-rays. Moreover, the benefits of bone removal, lung nodule detection, and others in dual-energy chest radiography have been proven useful.[24–26] A recent in vitro investigation of spectral photon-counting radiography (SPCR)[27] has shown promising results in the identification of crystals related to arthropathy, reviving interest in plain radiography for this diagnosis and its monitoring. Furthermore, dark-field radiography is also currently being investigated with respect to its usability for MSU detection.[28]

The purpose of this study was to test whether SPCR can distinguish and identify various crystal suspensions related to arthropathy by using a vendor-specific calibrated phantom and clinical DECT data

Received for publication June 7, 2020; and accepted for publication, after revision, July 10, 2020.

From the *Institute of Diagnostic and Interventional Radiology, University Hospital Zurich and Faculty of Medicine, University of Zurich, Zurich; †Department of Diagnostic and Interventional Radiology, Lausanne University Hospital, University of Lausanne, Lausanne; ‡DECTRIS Ltd, Baden; §Department of Orthopaedics and Traumatology, and ||University Institute of Pathology, Lausanne University Hospital, University of Lausanne, Lausanne, Switzerland.

S.G. and T.T. are full-time employees of Dectris Ltd, a company with headquarters in Switzerland that supported us with the detector prototype used for this investigation. The remainder of the authors have no conflicts of interest. All experimental settings and the study conduct were initiated by the scientific guarantor (R.G.) and by F.A.H. who have no affiliation with the aforementioned company.

Correspondence to: Florian Alexander Huber, MD, Institute of Diagnostic and Interventional Radiology, University Hospital Zurich and Faculty of Medicine, University of Zurich, Raemistrasse 100, 8091 Zurich, Switzerland. E-mail: florian.huber@usz.ch.

ISSN: 0020-9996/20/0000–0000
DOI: 10.1097/RLI.0000000000000717

as reference standard. Crystal identification was then validated on an excised human third left toe from a chronic gouty arthritis patient to prove possible clinical application of SPCR in vivo.

MATERIALS AND METHODS

Samples

Phantom

Industry standard samples of synthetic MSU, CPP, and HA crystals at 3 different concentrations mimicking in vivo conditions were used for all scans: 200, 400, and 600 mg/mL of MSU and 50, 100, and 150 mg/mL of CPP and HA, respectively. According to in vivo findings and empirical data from previous pilot studies, MSU at 200 mg/mL is a borderline concentration for positive gout detection in the default DECT postprocessing workflow. The maximum MSU concentration was the highest achievable value by the manufacturer for ensuring a homogeneous phantom. Calcium pyrophosphate and HA are known to be of higher attenuation; hence, their concentrations were adapted accordingly. The respective concentrations were considered as "low," "medium," and "high." All samples were available as same-sized calibration rods at a diameter of 5 mm each and homogeneous crystal concentrations (Fig. 1). The samples were obtained from a CE-certified and Food and Drug Administration–certified vendor for medical imaging phantoms (Computerized Imaging Reference Systems, Inc, Norfolk, VA).

Human Specimen

In addition, an ex vivo fresh (thawed at room temperature) anatomic specimen of the third toe of the left foot was harvested from a 65-year-old male patient with known chronic gouty arthritis who had surgical amputation of his limb performed as the ultimate therapeutic option. The presence of MSU was then confirmed by polarized light microscopy, and the specimen was subsequently scanned with SPCR in perpendicular standard views and with DECT with routine protocol for gout assessment of the foot. Written consent of the patient to use the biological material for scientific purposes was given before surgery. Institutional review board approval was waived, as data inclusion concerned less than 5 patients, in compliance with local and national ethics regulations.

SPCR Image Acquisition, Calibration, and Postprocessing

All samples were scanned using a microfocus source x-ray tube (Hamamatsu microfocus x-ray source L9181-02; Hamamatsu Photonics K.K., Hamamatsu, Shizuoka Prefecture, Japan), a standard 0.52-mm aluminum filter, and an industry-standard high-resolution PC detector prototype of the latest generation (blinded). Tube-detector distance and tube voltage were chosen similar to presets of a clinical standard radiograph and kept constant throughout all scans. The respective acquisition and image reconstruction parameters are listed in detail in Table 1. Because of the complexity of dose calculations under clinical conditions, we decided to estimate dose ranges only using a standard simulation tool,[29,30] instead of a systematic assessment. Based on a previous pilot study,[27] quantitative results of our SPCR setup did not differ significantly between low and high dose, given a range between 0.18 and 18 mAs (ie, 300 μA tube current over an exposure time of 60 seconds). For the parameters as stated in Table 1, the simulation output was an air kerma of 191 μGy/mAs. For our different exposure values, this value was multiplicated with the mAs, resulting in a dose estimate of 34.4 μGy up to 3.44 mGy. As the conversion to organ dose (Sievert) is difficult due to lack of organ-specific weighting factors at the appendicular skeleton, we compared our results with the clinical routine of 2 perpendicular radiographic projections of the hand. These examinations usually range approximately 1 to 5 mAs and were therefore considered comparable with regard to radiation dose of the SPCR setup used in this study.

Calibration was necessary before material decomposition and was performed with industry-standard pure plates in different

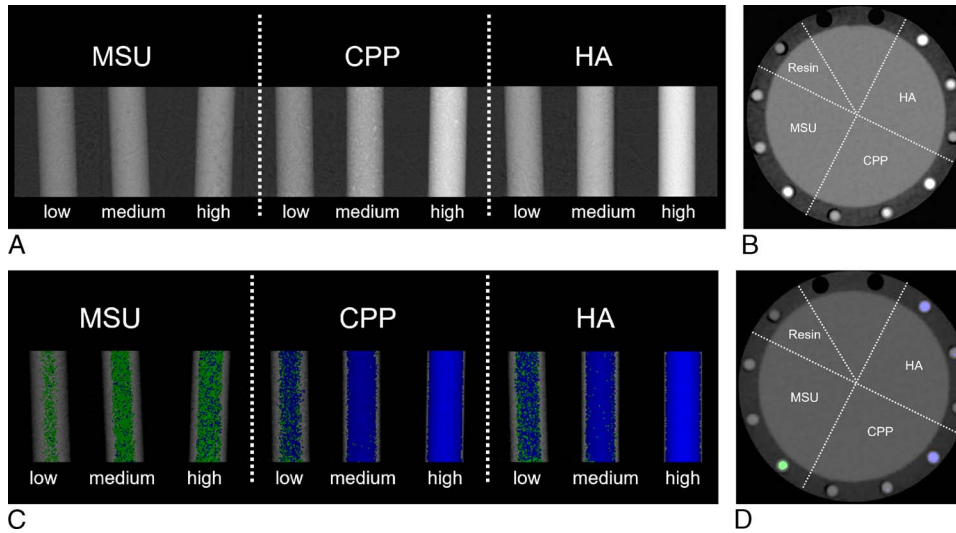

FIGURE 1. A–D, Cylindrical samples of monosodium urate (MSU), calcium pyrophosphate (CPP), and calcium hydroxyapatite (HA) in low, medium, and high concentration (as explained in the manuscript), examined by (A and B) spectral photon-counting radiography, from left to right, respectively. The samples are visualized in (A) a grayscale-coded absolute attenuation image and (B) a color-coded decomposition image. For better presentation, the images were postprocessed to fit in 1 line (from 2 separate scans with identical acquisition parameters). C and D, Images show the same cylindrical samples in representative axial images of DECT validation scan, where HA, CPP, and MSU are ordered clockwise, in decreasing concentration, respectively, starting at the 1-o'clock position. The last sample is a resin rod without any further additives. Panel C is a standard grayscale image (soft tissue kernel, mixed sources), whereas panel D was extracted from the vendor workflow for gout detection. Note that despite quite high concentration of MSU, CT is able to detect "tophi" only in the highest concentrated MSU rod, because of material separation by attenuation thresholding (>150 HU, clinically validated and vendor-recommended threshold).

TABLE 1. Scan Acquisition and Image Reconstruction Parameters in SPCR and in DECT

Parameter	SPCR	DECT
mAs	18	205/137
kVp	50	80/Sn150
Distances, source detector/source object, cm	100/90	NA, centered halfway
Energy bins, keV	15–25, 30–50	NA
Slice thickness/increment, mm	NA	1/1.5
Kernel	NA	Qr36
Field of view, mm	60 × 80	110
Pixel size, mm^2	0.15 × 0.15	0.215 × 0.215
Dose	0.18–18 mAs (dose simulation, 34.4 μGy to 3.44 mGy)	9.47 mGy ($CTDI_{vol}$)

SPCR, spectral photon-counting radiography; DECT, dual-energy computed tomography; NA, not available.

thicknesses of polyvinyl chloride (1–16 mm) and acrylic glass (polymethyl methacrylate; 2–48 mm).

Reconstructions were generated for energy windows of 15 to 25, 25 to 30, 30 to 35, and 35 to 50 keV. Image postprocessing for decomposed images and determination of Z_{eff} values was performed using the method described in the original research of Alvarez and Macovski[31] and Lehmann et al.[32]

Validation DECT Scans

All samples were additionally scanned with a DECT scanner of the latest generation (Siemens Force; Siemens Healthineers Inc, Erlangen, Germany) using the clinical standard protocol for gout assessment of peripheral joints (dual-source imaging with tube voltages at 80 kV and tin [Sn]–filtered 150 kV). For further acquisition and image reconstruction parameters, see Table 1.

Image postprocessing and measurements of Z_{eff} values were performed using the corresponding CE-certified vendor software for tophus detection (syngo.via CT Dual-Energy Gout; Siemens Healthineers Inc, Erlangen, Germany). Minimum thresholds for Z_{eff} analysis were set at the recommended clinical standard of 150 Hounsfield units (HUs).[8,9]

Quantitative Analysis

Narrow rectangular regions of interest (ROIs) at a defined size of 2 pixels width and 60 pixels length were placed over the middle aspect of the rods in the SPCR images to reduce the effects of the cylinder's thickness variation to extracted quantitative values. Round ROIs of 1 mm^2 (21 pixels) were placed in the central portions of the crystal rod cross-sectional area on 10 consecutive images in DECT-derived Z_{eff} maps series, respectively. Thereby, means and standard deviations of Z_{eff} values for among modalities, HU values, and dual-energy indices (DEIs) on DECT, as well as gray values (GVs) in SPCR were measured. Gray values were determined for each sample defined by $GV = -\log(I/I_0)$, where I and I_0 were the intensities in the x-ray images measured with and without object, respectively.

Statistical Analysis

Analysis of variance and post hoc Bonferroni correction for multiple comparisons were used for the evaluation of differences in Z_{eff}, DEI, and HU/GV among materials and concentrations in SPCR (GV only) and DECT measurements, respectively. Furthermore, analysis of variance was also used to test for material inhomogeneities among different measurement regions in the DECT-derived images. Student t testing was used to test for differences between SPCR and DECT. All scan results were processed with Excel (Microsoft Excel for Office 365 Version 1810; Microsoft Co, Redmond, WA), whereas SPSS was used for statistical analysis (IBM SPSS version 25; IBM Co, Armonk, NY). A P value below 0.05 was considered statistically significant.

RESULTS

Phantom

In SPCR, significant differences in GV and Z_{eff} values were found for different concentrations of each material (F = 760–11,320, $P < 0.001$ for all) and for different materials at matching concentrations (F = 840–7220, $P < 0.001$), respectively. For all samples, no significant differences were observed for Z_{eff} values among different DECT images in the central portions of the respective rods ($P = 1$).

In general, quantitative measurements in SPCR were comparable with findings on DECT images, where HU, DEI, and Z_{eff} values were also significantly different among all materials (F = 14.5–6187.6, all P's < 0.001) and among their respective concentrations per material (F = 56.4–50,697.2, all P's < 0.001), except when comparing HU values among Sn150kV images of all high concentration samples (F = 0.183, P = 0.834).

Comparing mean Z_{eff} values of identical concentrations and materials, no significant differences were found between SPCR and DECT, except for MSU in low concentration ($P < 0.05$) as well as CPP and HA in high concentrations ($P < 0.001$ for both).

A detailed overview of SPCR- and DECT-derived measurements of all crystal suspensions used and their respective concentrations is given in Table 2.

Although larger overlaps of materials were seen regarding GV, substantial differences between calcium-containing crystals (CPP and HA) and MSU were noted in the respective Z_{eff} and DEI values. Eventual differentiation by those discriminators was always possible for MSU versus CPP/HA, as Z_{eff} of the highest concentrations of MSU ranged markedly below the lowest concentrations of calcium-containing phantoms. The observed trends of attenuation behavior and Z_{eff} were comparable with findings in DECT (Fig. 2).

Human Specimen

Visual analysis in SPCR of the anatomic specimen showed typical bone erosions in the gout-affected distal interphalangeal joint of the third left toe in grayscale radiographic images, yet without clear depiction of MSU gouty tophi. Image decomposition of SPCR with color coding of highly attenuating (GV > 0.90) materials with a Z_{eff} ranging between 6 and 8 as green revealed presence and extent of MSU deposits mostly concordant with DECT. Because we chose a very high attenuation cutoff in SCPR color-coded images, disease extent was considered to be depicted with good specificity but reduced visual sensitivity compared with the vendor default setup of DECT postprocessing. This is,

TABLE 2. GVs/HU Values As Well as Z_{eff} Values for All Samples in SPCR Test Setting and From Clinical Standard DECT Scan as Reference Standard

Parameter	Resin	MSU Low	MSU Mid	MSU High	CPP Low	CPP Mid	CPP High	HA Low	HA Mid	HA High
GV SPCR	0.18 ± 0.01	0.20 ± 0.01	0.23 ± 0.01	0.25 ± 0.01	0.24 ± 0.01	0.30 ± 0.02	0.44 ± 0.02	0.25 ± 0.01	0.31 ± 0.01	0.44 ± 0.01
HU DECT 80 kV	−10.9 ± 3.4	62.5 ± 5.8	67.9 ± 1.4	183.8 ± 39.5	84.6 ± 2.3	180.2 ± 5.1	354.6 ± 2.8	87.0 ± 2.1	176.7 ± 1.8	371.3 ± 2.2
HU DECT Sn150kV	−40.0 ± 3.4	107.2 ± 4.6	111.5 ± 3.6	211.0 ± 42.4	82.6 ± 1.7	127.7 ± 3.2	205.3 ± 3.4	79.8 ± 3.5	131.2 ± 6.5	211.1 ± 3.4
DECT dual-energy index	−0.025 ± 0.002	−0.021 ± 0.002	−0.020 ± 0.002	−0.011 ± 0.002	0.001 ± 0.002	0.023 ± 0.002	0.058 ± 0.002	0.003 ± 0.003	0.020 ± 0.003	0.062 ± 0.002
Z_{eff} SPCR	5.41 ± 0.70	6.05 ± 0.58	6.42 ± 0.59	6.80 ± 0.36	7.22 ± 0.52	8.58 ± 0.78	10.43 ± 0.82	7.74 ± 0.65	8.48 ± 0.51	10.37 ± 0.72
Z_{eff} DECT	6.29 ± 0.11	6.52 ± 0.09	6.55 ± 0.08	6.96 ± 0.08	7.47 ± 0.08	8.30 ± 0.07	9.47 ± 0.05	7.57 ± 0.09	8.20 ± 0.12	9.56 ± 0.05

Additional dual-energy indices were retrieved from the DECT post-processing workflow. Values indicate mean and standard deviation for measurements in a region of interest with constant size.
GV, gray value; SPCR, spectral photon-counting radiography; DECT, dual-energy computed tomography; MSU, monosodium urate; CPP, calcium pyrophosphate; HA, calcium hydroxyapatite.

however, a product of arbitrary color coding independent from true quantitative calculations. Postimaging validation by gross pathology and histology confirmed the distribution pattern of gout tophi, whereas polarized light microscopy confirmed the presence of MSU (Fig. 3).

DISCUSSION

This proof-of-concept study shows that identification and discrimination of different concentrations of arthropathy-related crystals are feasible with SPCR at comparable diagnostic accuracy to DECT. In this study, beyond the identification of 3 crystal materials and concentrations in a high-end industry phantom, subcutaneous and intraosseous (ie, within a gouty bone erosion) MSU deposits in and around the distal interphalangeal joint of an excised human third left toe could also be identified for the first time with SPCR, as confirmed by gross pathology, histology, and polarized light microscopy. To the best of our knowledge, this is the first description of the use of PC detectors in radiography for this clinical application in the scientific literature.

This finding is concordant with and supported by our recently performed initial study that suggested the ability of crystal differentiation with SPCR.[27] However, this previous purely in vitro experiment included only 2 materials (MSU and HA), and quantitative results were based on own-built suspensions with subsequent crystal suspension heterogeneity. Distinguishing between MSU and other crystal-associated arthropathies can be effectively performed using DECT. This technique is already well described and hence established clinically.[4,5,33] Dual-energy computed tomography is usually performed to exclude subcutaneous tophi in patients with high disease pretest probability and/or negative microscopic results from synovial fluid aspiration, and to assess crystal burden in known chronic gouty arthritis patients.[4,6] On the other hand, the widespread availability and good reproducibility of ultrasound for gout assessment,[34] despite the relative lack of specificity, further limit the spectrum of indications for DECT. Eventually, considering that DECT scans of a single extremity region imply a dose increase by at least a hundredfold compared with a standard biplanar radiography,[35,36] the latter would be an interesting modality for screening—voluntary or opportunistic—and disease monitoring of crystal-associated arthropathies, providing adequate identification of crystal nature.

With this proof-of-concept study, we demonstrate the possible identification and differentiation of crystals in SPCR beyond visual assessment based on plain attenuation (GV) but with additional information on crystal nature based on Z_{eff}. Although larger overlaps of materials were seen regarding GV, substantial differences between calcium-containing crystals (CPP and HA) and MSU were noted in the respective Z_{eff} values and consequently with DEI in DECT, respectively. The latter reflects a material specific index that puts into relation the attenuation behavior at 2 different tube potentials, that is, HU values at 80 kV and Sn150kV.

In addition, Z_{eff} values derived from SPCR were highly concordant with reference standard DECT derived values, except for MSU in low concentration ($P < 0.005$) as well as CPP and HA in high concentrations ($P < 0.001$ for both). At first, this finding suggests reduced accuracy in the highest and lowest Z_{eff} samples of crystal suspensions but may be explained by 2 reasons: first, despite using state-of-the-art methods and well-accepted algorithms for prior calibration, it is known that consideration of areal densities (ie, density × thickness in grams per centimeter square) plays an essential role in Z_{eff} accuracy. Although our calibration materials were acrylic glass (areal density, 0.24) and polyvinyl chloride (0.14), areal density of different MSU and HA/CPP concentrations ranged somewhere around 0.1 to 0.3 (low to high concentration) and 0.025 to 0.075, respectively. This perfectly matches with the reduced comparability of low concentrated MSU, which was of slightly lower areal density than the calibration materials, but also partly HA/CPP, which ranked comparably farer off the calibration range. It is common practice to apply extrapolation from the calibration data for measurements outside range; however, this is naturally associated with

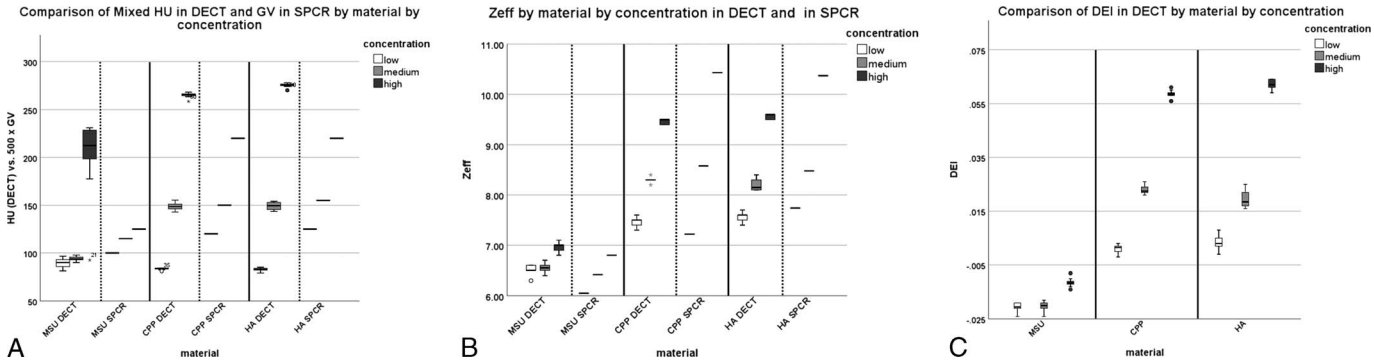

FIGURE 2. Comparison of quantitative attenuation descriptors of monosodium urate (MSU), calcium pyrophosphate (CPP), and calcium hydroxyapatite (HA), measured by dual-energy CT (DECT) and by spectral photon-counting radiography (SPCR). Panel A compares the Hounsfield units (HUs; Mixed kV image of routine gout postprocessing workflow) with SPCR-derived gray values (GVs; defined as written in the methods section). For better visual comparability, GVs were multiplied by 500. In B, Z_{eff} of both modalities are compared. Panel C compares dual-energy indices (DEIs) from DECT scans of all materials and concentrations. All DECT measurements were performed at 10 consecutive images and are presented with usual boxplots. The SPCR-related measurements represent the mean value of the continuous total measurement area.

larger errors/biases. Second, despite high homogeneity of crystal rods and ROI measurements with maximum precision for delineation and thickness calibration in SPCR, ROI widths of only 2 pixels because of cylindric rod dimensions may be prone to measurement bias as compared with 3D image information from DECT.

The SPCR technique supplements high-resolution spatial information from conventional radiography with material decomposition from multienergy imaging. A Z_{eff}-based material decomposition per se would also technically be possible with DE radiography.[37] Yet, several benefits come along with the utilization of PC technique, compared with DE. Photon-counting detector can ensure minimal dose to the patient while producing sharper images because of direct conversion sensors. Furthermore, different to most DE techniques, patient motion–related image blurring is usually not an issue in SPCR. The use of more than 2 energy bins may in addition lead to better specificity in material discrimination and allow for future settings of multicontrast agent examinations.[12,38,39] Some of these findings have already been investigated, and our results in general concur with previous CT studies from Kirkbride et al[11] and Stamp et al,[12] who have proved increased accuracy of material discrimination using PC-CT instead of DECT. Also, for other reasons, such as excellent spatial resolution because of a reduction in image noise, PC detectors are increasingly being investigated for CT imaging,[40] and they are widely recognized as key components for personalized functional imaging in the near future.[41] Furthermore, Stamp et al[12] have similarly demonstrated visible differences in the extent of MSU between DECT and spectral PC-CT, as was also clearly shown in our

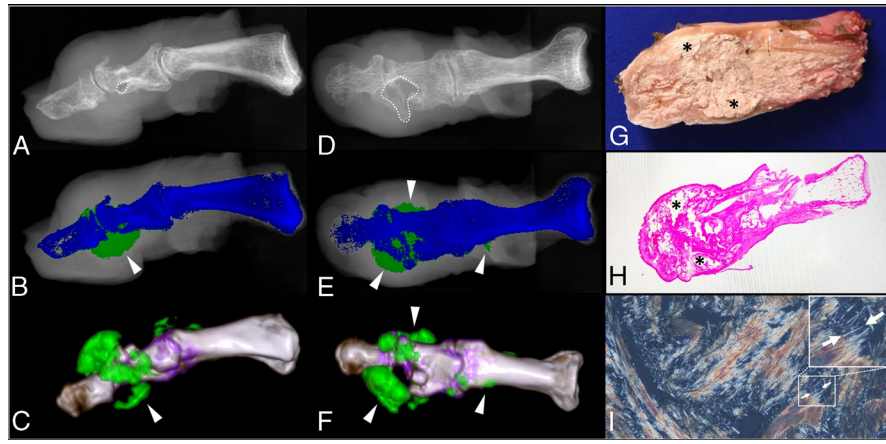

FIGURE 3. Comparison of grayscale spectral photon-counting radiography (SPCR) images (A and D), Z_{eff} color-coded SPCR images (B and E), as well as volume-rendered 3D reconstructions of validating dual-energy CT scans (C and F) in panels A to C lateral and panels D to F dorso-palmar views of an ex vivo third left toe (anatomic cadaver specimen) from a 65-year-old male patient with known history of chronic gouty arthritis. The images clearly show disease-typical bony erosions (exemplary dotted lines in A and D). In comparison, color-coded images (B and E, C and F), photograph of pathologic dissection (G), as well as exemplary histologic hematoxylin and eosin stain (H) reveal significantly larger disease extent. Panels B and E are overlaps of a standard grayscale visualization and a color-coded mask, which labels all highly attenuating structures with effective atomic numbers within the range of monosodium urate (MSU; ie, tophi; green; arrowheads). The periarticular opacities can be clearly identified as gout manifestations. Corresponding green areas were seen in CT (arrowheads in C and F) and in photographs as yellow tophaceous tissue during dissection (G, asterisks), which left typical "washed out" spots after staining (H, also asterisks). The criterion standard of (I) polarized light microscopy confirmed the extensive presence of MSU crystals; in the right upper corner of the panel, a magnified area shows an exemplary singular crystal (white arrows). The difference in MSU extent between SPCR and DECT is owed to currently missing thresholds for minimum attenuation cutoffs, as established by diagnostic accuracy studies. The authors chose the DECT setting as recommended by the vendor, whereas the SPCR color setting was chosen arbitrarily, and it was considered to match most optimally with the criterion standard of anatomic resection, that is, not overexaggerating disease extent.

investigation (Fig. 3). This may further highlight the clinical need and importance of novel modalities for correct crystal identification and quantification in gout and related conditions.

The limitations of this study are inherent to its experimental design. Although the used medical imaging phantom was of high quality and crystal compounds were homogeneously fabricated, in vivo conditions may be more heterogeneous with even mixed deposits, that is, coexisting MSU and calcium crystals.[42] However, simulated conditions should rather reflect limits of reference range to extrapolate to real in vivo conditions. Although we were able to reliably differentiate compounds in all phantom and human specimen scans and could visually identify crystalline MSU regions from possible confounders, we did not investigate the impact of material overlay. Surrounding soft tissue is known to have comparable Z_{eff} to MSU and can suggest high attenuation on superimposed views. This may also result in inferior sensitivity and specificity of SPCR compared with cross-sectional imaging with DECT or PC-CT. Further, at present, SPCR is dependent on quite expensive high-end detectors that allow for identification of different photon energies. Moreover, the detector in use was a prototype built with a comparably small field of view. To reach broad acceptance, clinical applicability and costs of this technique using larger detectors and fast postprocessing will be crucial. Ideally, solutions should be sought that allow to upgrade preexisting conventional radiography units with SPCR detectors, thereby introducing the additional benefit of material decomposition to conventional radiography with minor efforts.

In conclusion, both in vitro and ex vivo identification and differentiation of crystals related to arthropathies are possible with SPCR at comparable diagnostic accuracy to DECT. Further research is needed to assess diagnostic accuracy and clinical usability of this new technique in vivo in clinical routine.

REFERENCES

1. Richette P, Doherty M, Pascual E, et al. 2016 updated EULAR evidence-based recommendations for the management of gout. *Ann Rheum Dis*. 2017;76:29–42.
2. McGill NW. Gout and other crystal-associated arthropathies. *Baillieres Best Pract Res Clin Rheumatol*. 2000;14:445–460.
3. Dalbeth N, Merriman TR, Stamp LK. Gout. *Lancet*. 2016;388:2039–2052.
4. Richette P, Doherty M, Pascual E, et al. 2018 updated European League Against Rheumatism evidence-based recommendations for the diagnosis of gout. *Ann Rheum Dis*. 2020;79:31–38.
5. Neogi T, Jansen TL, Dalbeth N, et al. 2015 gout classification criteria: an American College of Rheumatology/European League Against Rheumatism collaborative initiative. *Arthritis Rheumatol*. 2015;67:2557–2568.
6. Bongartz T, Glazebrook KN, Kavros SJ, et al. Dual-energy CT for the diagnosis of gout: an accuracy and diagnostic yield study. *Ann Rheum Dis*. 2015;74:1072–1077.
7. Gamala M, Jacobs JWG, van Laar JM. The diagnostic performance of dual energy CT for diagnosing gout: a systematic literature review and meta-analysis. *Rheumatology (Oxford)*. 2019;58:2117–2121.
8. Gerster JC, Landry M, Duvoisin B, et al. Computed tomography of the knee joint as an indicator of intraarticular tophi in gout. *Arthritis Rheum*. 1996;39:1406–1409.
9. Gerster JC, Landry M, Dufresne L, et al. Imaging of tophaceous gout: computed tomography provides specific images compared with magnetic resonance imaging and ultrasonography. *Ann Rheum Dis*. 2002;61:52–54.
10. Strobl S, Kremser C, Taljanovic M, et al. Impact of dual-energy CT postprocessing protocol for the detection of gouty arthritis and quantification of tophi in patients presenting with podagra: comparison with ultrasound. *AJR Am J Roentgenol*. 2019;213:1315–1323.
11. Kirkbride TE, Raja AY, Müller K, et al. Discrimination between calcium hydroxyapatite and calcium oxalate using multienergy spectral photon-counting CT. *AJR Am J Roentgenol*. 2017;209:1088–1092.
12. Stamp LK, Anderson NG, Becce F, et al. Clinical utility of multi-energy spectral photon-counting computed tomography in crystal arthritis. *Arthritis Rheumatol*. 2019;71:1158–1162.
13. Ren L, Zheng B, Liu H. Tutorial on x-ray photon counting detector characterization. *J Xray Sci Technol*. 2018;26:1–28.
14. Willemink MJ, Persson M, Pourmorteza A, et al. Photon-counting CT: technical principles and clinical prospects. *Radiology*. 2018;289:293–312.
15. Biswas D, Bible JE, Bohan M, et al. Radiation exposure from musculoskeletal computerized tomographic scans. *J Bone Joint Surg Am*. 2009;91:1882–1889.
16. Lell MM, Kachelrieß M. Recent and upcoming technological developments in computed tomography: high speed, low dose, deep learning, multienergy. *Invest Radiol*. 2020;55:8–19.
17. Rajendran K, Voss BA, Zhou W, et al. Dose reduction for sinus and temporal bone imaging using photon-counting detector CT with an additional tin filter. *Invest Radiol*. 2020;55:91–100.
18. Zhou W, Bartlett DJ, Diehn FE, et al. Reduction of metal artifacts and improvement in dose efficiency using photon-counting detector computed tomography and tin filtration. *Invest Radiol*. 2019;54:204–211.
19. Eriksson T, Berg P, Olerud C, et al. Low-dose CT of postoperative pelvic fractures: a comparison with radiography. *Acta Radiol*. 2019;60:85–91.
20. Gheno R, Nectoux E, Herbaux B, et al. Three-dimensional measurements of the lower extremity in children and adolescents using a low-dose biplanar x-ray device. *Eur Radiol*. 2012;22:765–771.
21. Kupfer S, Winklhofer S, Becker AS, et al. Gouty arthritis: can we avoid unnecessary dual-energy CT examinations using prior radiographs? *PLoS One*. 2018;13:e0200473.
22. Zhang W, Doherty M, Bardin T, et al. European League Against Rheumatism recommendations for calcium pyrophosphate deposition. Part I: terminology and diagnosis. *Ann Rheum Dis*. 2011;70:563–570.
23. De Silvestro A, Martini K, Becker AS, et al. Postoperative imaging of orthopaedic hardware in the hand and wrist: is there an added value for tomosynthesis? *Clin Radiol*. 2018;73:214.e1–214.e9.
24. Kuhlman JE, Collins J, Brooks GN, et al. Dual-energy subtraction chest radiography: what to look for beyond calcified nodules. *Radiographics*. 2006;26:79–92.
25. Manji F, Wang J, Norman G, et al. Comparison of dual energy subtraction chest radiography and traditional chest x-rays in the detection of pulmonary nodules. *Quant Imaging Med Surg*. 2016;6:1–5.
26. Ansari-Gilani K, Tandon YK, Jordan DW, et al. Dual-energy subtraction chest radiography: application in cardiovascular imaging. *J Thorac Imaging*. 2020;35:W75–W81.
27. Huber FA, Gkoumas S, Thüring T, et al. Detection and characterization of monosodium urate and calcium hydroxyapatite crystals using spectral photon-counting radiography: a proof-of-concept study. *Eur J Radiol*. 2020;129:109080.
28. Braig EM, Roiser N, Kimm MA, et al. X-ray dark-field radiography: potential for visualization of monosodium urate deposition. *Invest Radiol*. 2020;55:494–498.
29. Poludniowski GG, Evans PM. Calculation of x-ray spectra emerging from an x-ray tube. Part I. electron penetration characteristics in x-ray targets. *Med Phys*. 2007;34:2164–2174.
30. Poludniowski GG. Calculation of x-ray spectra emerging from an x-ray tube. Part II. X-ray production and filtration in x-ray targets. *Med Phys*. 2007;34:2175–2186.
31. Alvarez RE, Macovski A. Energy-selective reconstructions in x-ray computerized tomography. *Phys Med Biol*. 1976;21:733–744.
32. Lehmann LA, Alvarez RE, Macovski A, et al. Generalized image combinations in dual KVP digital radiography. *Med Phys*. 1981;8:659–667.
33. Newberry SJ, FitzGerald JD, Motala A, et al. Diagnosis of gout: a systematic review in support of an American College of Physicians Clinical Practice Guideline. *Ann Intern Med*. 2017;166:27–36.
34. Gruber M, Bodner G, Rath E, et al. Dual-energy computed tomography compared with ultrasound in the diagnosis of gout. *Rheumatology (Oxford)*. 2014;53:173–179.
35. Chou H, Chin TY, Peh WC. Dual-energy CT in gout - a review of current concepts and applications. *J Med Radiat Sci*. 2017;64:41–51.
36. American College of Radiology. Radiation Dose to Adults From Common Imaging Examinations. 2018. Available at: https://www.acr.org/-/media/ACR/Files/Radiology-Safety/Radiation-Safety/Dose-Reference-Card.pdf. Accessed August 7, 2020.
37. Sung JS, Lebron L, Keating D, et al. Performance of dual-energy contrast-enhanced digital mammography for screening women at increased risk of breast cancer. *Radiology*. 2019;293:81–88.
38. McCollough CH, Leng S, Yu L, et al. Dual- and multi-energy CT: principles, technical approaches, and clinical applications. *Radiology*. 2015;276:637–653.
39. Tao S, Rajendran K, McCollough CH, et al. Feasibility of multi-contrast imaging on dual-source photon counting detector (PCD) CT: an initial phantom study. *Med Phys*. 2019;46:4105–4115.
40. Klein L, Dorn S, Amato C, et al. Effects of detector sampling on noise reduction in clinical photon-counting whole-body computed tomography. *Invest Radiol*. 2020;55:111–119.
41. Alkadhi H, Euler A. The future of computed tomography: personalized, functional, and precise. *Invest Radiol*. 2020. doi:10.1097/RLI.0000000000000668. [published online ahead of print].
42. Hajri R, Hajdu SD, Hügle T, et al. Dual-energy computed tomography for the noninvasive diagnosis of coexisting gout and calcium pyrophosphate deposition disease. *Arthritis Rheumatol*. 2019;71:1392.